SCIENTIFIC REP♦RTS

Ultrasmall Fe$_2$O$_3$ nanoparticles/ MoS$_2$ nanosheets composite as high-performance anode material for lithium ion batteries

Bin Qu[1,2], Yue Sun[1], Lianlian Liu[1], Chunyan Li[1], Changjian Yu[1], Xitian Zhang[2] & Yujin Chen[1]

Coupling ultrasmall Fe$_2$O$_3$ particles (~4.0 nm) with the MoS$_2$ nanosheets is achieved by a facile method for high-performance anode material for Li-ion battery. MoS$_2$ nanosheets in the composite can serve as scaffolds, efficiently buffering the large volume change of Fe$_2$O$_3$ during charge/discharge process, whereas the ultrasmall Fe$_2$O$_3$ nanoparticles mainly provide the specific capacity. Due to bigger surface area and larger pore volume as well as strong coupling between Fe$_2$O$_3$ particles and MoS$_2$ nanosheets, the composite exhibits superior electrochemical properties to MoS$_2$, Fe$_2$O$_3$ and the physical mixture Fe$_2$O$_3$+MoS$_2$. Typically, after 140 cycles the reversible capacity of the composite does not decay, but increases from 829 mA h g^{-1} to 864 mA h g^{-1} at a high current density of 2 A g^{-1}. Thus, the present facile strategy could open a way for development of cost-efficient anode material with high-performance for large-scale energy conversion and storage systems.

Owing to their high energy densities and environmental benignity, lithium ion batteries (LIBs) have been used as potential power sources for various electronic devices and equipments, ranging from a tiny music player to a massive sports car[1,2]. However, the commercial graphite anode of LIBs is difficult to satisfy the requirements of high power equipment of the modern society due to its low specific capacity (372 mAh g^{-1}). Thus, alternative anode materials with good electrochemical performances are particularly desirable. 2H-MoS$_2$, as a typical member of transition metal dichalcogenides, is composed of a layer of molybdenum atoms sandwiched between two layers of sulphur atoms. The spacing between neighboring layers is 0.615 nm, significantly larger than that of graphite (0.335 nm), and the weak van der Waals forces between the layers allows Li ions to diffuse without a significant increase in volume, leading to high-performance of MoS$_2$ as anode material than that of graphite[3]. The theoretical capacity of MoS$_2$ is as high as 670 mAh g^{-1}, resulting from a conversion reaction of $MoS_2 + 4Li^+ + 4e^- \rightarrow Mo + 2Li_2S$[4,5]. Furthermore, MoS$_2$ surface exists many unsaturated sulfur dangling bonds, which will also be involved in the charge and discharge reactions[6], and consequently the actual capacity of MoS$_2$ is often higher than the theoretical value[7–9]. Recently, in order to improve the reversible capacity of MoS$_2$ many strategies were developed to synthesize various MoS$_2$ nanostructures including exfoliated MoS$_2$[10] and hollow MoS$_2$ nanosheet assemblies, nanotubes[11,12], nanoboxes[13,14], MoS$_2$@void@MoS$_2$[15], and hollow nanospheres[16,17]. Unfortunately, due to the poor conductivity, the MoS$_2$ materials exhibited inferior cycling stability and rate performance, which impedes their practical application[10]. One efficient solution is to introduce carbon materials, such as graphene nanosheets[18–29], carbon nanotubes[30–32], carbon nanospheres[33], carbon fiber cloth[34,35], mesoporous carbon[36] to improve the electrical conductivity of the composite materials. However, due to the lower capacity of these carbon materials, the overall energy density of the composite material would be suppressed.

Because of its high theoretical capacity (1005 mA h g^{-1}), low cost, abundance in nature, and environmental benignity Fe$_2$O$_3$ is another promising anode material[37,38]. Especially when Fe$_2$O$_3$ in ultrasmall size (5~10 nm) can exhibit high rate electrochemical performances[37,38]. Firstly, the ultrasmall size can greatly mitigate the volume expansion/contraction of Fe$_2$O$_3$ particles during charge/discharge. Secondly, a high lithium ion flux can be

[1]Key Laboratory of In-Fiber Integrated Optics, Ministry of Education and College of Science, Harbin Engineering University, Harbin 150001, China. [2]Key Laboratory for Photonic and Electronic Bandgap Materials, Ministry of Education and School of Physics and Electronic Engineering, Harbin Normal University, Harbin 150025, China. Correspondence and requests for materials should be addressed to C.L. (email: chunyanli@hrbeu.edu.cn) or Y.C. (email: chenyujin@hrbeu.edu.cn)
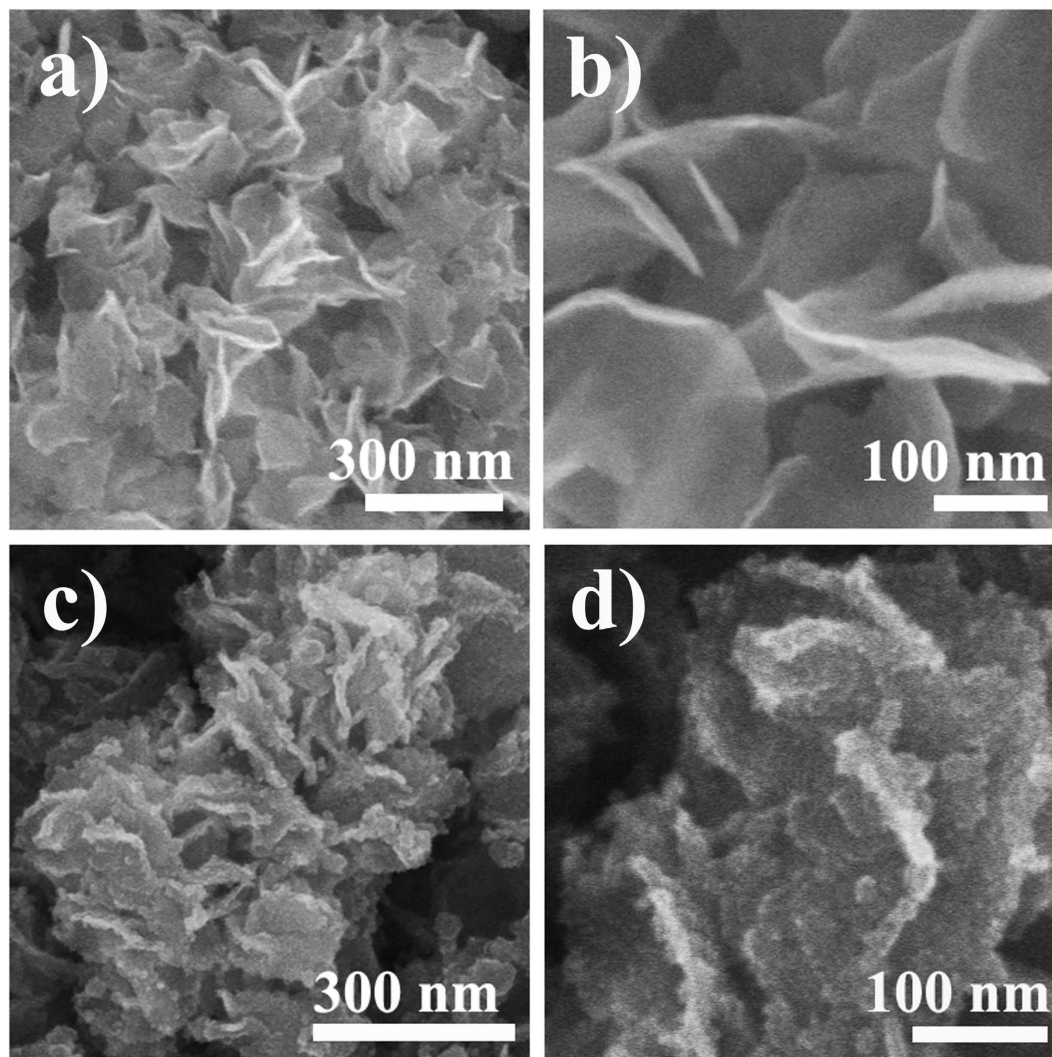
Figure 1. Structrual characterization of MoS$_2$ nanosheets and Fe$_2$O$_3$/MoS$_2$ composite. (a,b) SEM of MoS$_2$ nanosheets, and **(c,d)** SEM of Fe$_2$O$_3$/MoS$_2$ composite.

achieved by the large surface area provided by the ultrasmall particles[39]. More importantly, due to the extremely short distance for lithium ions transportation within ultrasmall particles, the rate capability of lithium insertion/removal can be significantly enhanced[40]. However, the nanostructured Fe$_2$O$_3$ exhibited a poor cycling stability due to structural damage during charging/discharging process[37].

Herein, we report a facile method to grow ultrasmall Fe$_2$O$_3$ nanoparticles on 2H-MoS$_2$ nanosheets, where MoS$_2$ nanosheets in the composite can serve as scaffolds, efficiently buffering the large volume changes of Fe$_2$O$_3$ during charging/discharging process, whereas the ultrasmall Fe$_2$O$_3$ nanoparticles mainly provide the specific capacity of the anode as well as the enhanced electrical conductivity. Furthermore, strong coupling between Fe$_2$O$_3$ and MoS$_2$ nanosheets, elucidated by X-ray photoelectron spectrum measurements, facilitates a rapid charge transfer. In addition, MoS$_2$ nanosheets in the composite can also contribute to the total capacity of the anode. As a consequence, the composite prepared here exhibited superior electrochemical performance for anode material for Li-ion battery.

Results

SEM images (Fig. 1a and b) show that the as-prepared MoS$_2$ exhibits sheet-like morphology with a thickness and a lateral length of about 10 and 400 nm, respectively, similar to that reported previously[41]. After Fe$_2$O$_3$ coating, the MoS$_2$ exhibits a similar morphology and lateral length to that of the pristine MoS$_2$ nanosheets, but the surface becomes drastically rough (Fig. 1c), in sharp contrast to the smooth surface of the pristine MoS$_2$ nanosheets (Fig. 1b). From the high-magnification SEM image of the composite (Fig. 1d)), it can also be found that many ultrasmall particles are anchored on both sides of basal planes of MoS$_2$ nanosheets. Figure 2a shows a TEM image taken from the basal plane of MoS$_2$ nanosheets in the composite. It can be found that Fe$_2$O$_3$ nanoparticles are uniformly and densely deposited on the surface of the MoS$_2$ nanosheets. The size distribution plot (Figure S1) indicates that the average size of Fe$_2$O$_3$ nanoparticles is about 4.0 nm. Most lattice fringes of the Fe$_2$O$_3$ nanoparticles in the high-resolution TEM (HRTEM) image (Fig. 2b) are not resolved well, revealing the weak degree of
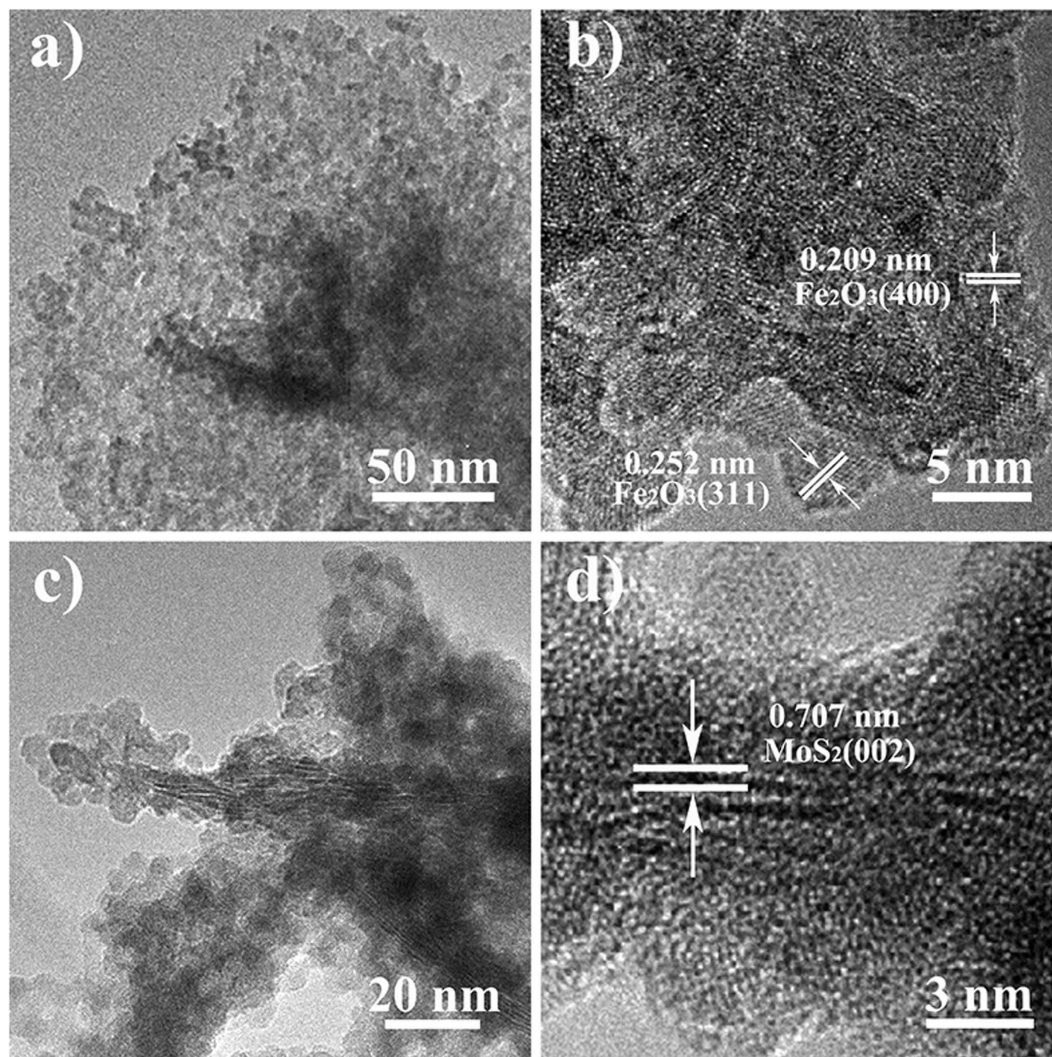
Figure 2. TEM image of Fe₂O₃/MoS₂ composite. (**a,b**) TEM and HRTEM images taken from basal plane, and (**c,d**) cross-section TEM and HRTEM image of basal plane.

crystallizations of the Fe_2O_3 nanoparticles. The labeled lattice spacing for Fe_2O_3 nanoparticles in the HRTEM image is about 0.209 nm and 0.252 nm, which can be assigned to the (400) plane and (311) plane of Fe_2O_3, respectively. The fast Fourier transformation (FFT) technique confirms the crystal nature of Fe_2O_3 on the MoS_2 nanosheets (Figure S2). Cross-section TEM image (Fig. 2c) reveals that the utrasmall Fe_2O_3 nanoparticles mainly disperse on the basal planes of the MoS_2 nanosheets, in which the lattice fringes corresponding to (002) plane can be clearly observed. HRTEM image (Fig. 2d) reveals that the interlayer distance of the (002) plane of the MoS_2 nanosheets is about 0.707 nm, larger than the value (0.615 nm) of bulk MoS_2.

The crystal structures of the samples were examined using X-ray diffraction (XRD) measurement. Figure 3a shows the XRD pattern of the pristine MoS_2 nanosheets, in which the peaks located at $2\theta = 32.2°$ corresponds to the (100) and (101) planes, $2\theta = 38.3°$ corresponds to the (103) plane and the peaks located at $2\theta = 57.3°$ corresponds to the (110) and (008) planes of 2H-MoS_2 (JCPDS No. 37–1492). Compared to 2H-MoS_2 bulk, these peaks slightly shift toward low-angle region, revealing the slightly enlarged lattice distances along the basal planes of 2H-MoS_2. Similar to the previous report[41], two additional peaks located at 9.2° and 18.5°, marked by "#", are also observed at low-angle region. The corresponding d-spacings calculated according to the Bragg equation are 0.96 and 0.48 nm, respectively. The diploid relation between the d-spacings reveals that the MoS_2 nanosheets possess a new lamellar structure with a larger interlayer spacing of 0.96 nm than that of 0.615 nm in bulk 2H-MoS_2[34,41,42]. The enlarged interlayer spacing may be related to the synthesis conditions[28,34,41,42]. As previously reported[41], when the temperature was lower than 180 °C, the MoS_2 nanosheets with enlarged interlayer spacing (0.95 nm) could be obtained in alkaline media; while the temperature was increased to 220 °C, the interlayer distance of the nanosheets kept the same value as that in bulk MoS_2[41]. On the other hand, the enlarged interlayer spacing could be achieved in the media containing urea at 220 °C; however, when the pH in the media was decreased by replacing urea with ammonium fluoride, even at the same temperature the phenomenon did not occur[42]. Therefore, the alkalinity and the synthetic temperature seriously affect the interlayer distance of the MoS_2 nanosheets. Under
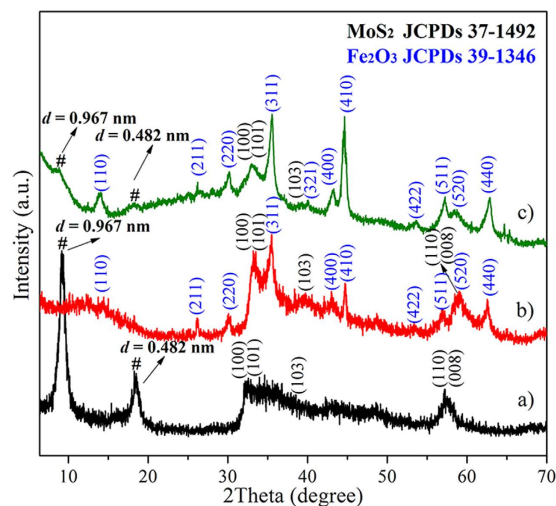
Figure 3. XRD patterns. (**a**) MoS_2 nanosheets, (**b**) Fe_2O_3/MoS_2 composite and (**c**) the physical mixture $Fe_2O_3+ MoS_2$.

the experimental conditions such as strong alkaline media and low temperature, oxygen species may incorporate more easily with MoS_2, leading to the different lamellar structure with a enlarged interlayer spacing than that of 0.615 in bulk 2H-MoS_2[34,41,42]. However, the new lamellar structure is thermodynamically unstable. After annealing the MoS_2 nanosheets at 500 °C for 3 h under an Ar flow, XRD analysis was carried out. As shown in Figure S3, the diffraction peaks at 9.2° and 18.5° disappear, while all the resolved peaks can be assigned to thermodynamically stable 2H-MoS_2 (JCPDS No. 37–1492). After Fe_2O_3 coating, the peak corresponding to the (002) plane is suppressed significantly, further suggesting that uniform and dense nanoparticles are deposited on the both sides of the basal plane of the MoS_2 nanosheets (Fig. 3b). In addition, the peaks from the Fe_2O_3 and MoS_2 can also be identified in the XRD pattern. The diffraction peaks at $2\theta = 33.4°$ can be assigned to (100) and (101) planes, $2\theta = 39.5°$ can be assigned to (103) plane and $2\theta = 58.5°$ can be assigned to (110) and (008) planes of 2H-MoS_2, respectively, whereas those at $2\theta = 14.5°$, 26.1°, 30.2°, 35.5°, 43.2°, 44.6°, 53.6°, 57.1°, 59.6° and 62.7° can be indexed to (110), (211), (220), (311), (400), (410), (422), (511), (520) and (440) planes of Fe_2O_3 (JCPDS no. 39–1346), respectively. Notably, the peak position of (110) plane in Fig. 3a is different from that in Fig. 3b. This is because the pristine MoS_2 nanosheets with the enlarged interlayer spacing are thermodynamically unstable phases, while the MoS_2 nanosheets in Fe_2O_3/MoS_2 composite, which were annealing at 500 °C for 3 h under an Ar flow, are thermodynamically stable. They had different lamellar structures, leading to significantly difference in XRD results (Fig. 3 and Figure S4). Compared to the XRD pattern of the annealed MoS_2 nanosheets with that of the Fe_2O_3/MoS_2 composite, the peak position of (110) plane is almost identical (Figure S5). The above results demonstrate that crystalline Fe_2O_3 nanoparticles are successfully anchored on the surface of MoS_2 nanosheets. Figure 3c) shows the XRD pattern of the physical mixture $Fe_2O_3 + MoS_2$, in which the diffraction peaks from both Fe_2O_3 and MoS_2 can be observed. Notably, the diffraction peak corresponding to expanded (002) plane of MoS_2 nanosheets is still visible, significantly different from that of the Fe_2O_3/MoS_2 composite.

X-ray photoelectron spectroscopy (XPS) analysis was carried out to determine surface chemical compositions and valence states of the Fe_2O_3/MoS_2 composite and the MoS_2 nanosheets. Figure 4a shows the high-resolution XPS spectra of Mo 3d core level for the two samples. Two peaks at 231.9 eV and 228.7 eV are observed in the Mo 3d spectrum of the MoS_2 nanosheets, corresponding to Mo^{4+} species. After coating Fe_2O_3, the two peaks shift to high binding energy side by an approximately 0.3 eV. The shift of the binding energy indicates that electron transfer from MoS_2 to Fe_2O_3 occurs. It can be concluded that the strong coupling between MoS_2 and Fe_2O_3 is presented in the composite. However, such shift in the physical mixture $MoS_2+Fe_2O_3$ does not occur (Figure S6), revealing the advantage of our method for preparation of the Fe_2O_3/MoS_2 composite. In addition, two additional peaks at 235.6 eV and 232.5 eV are assigned to Mo^{6+} species[43–45], suggesting the surface oxidization of MoS_2 due to the electron transfer. In the XPS spectrum of S 2p core level for the pure MoS_2 nanosheets, the main doublet located at binding energies of 161.6 and 162.9 eV correspond to the S $2p_{3/2}$ and S $2p_{1/2}$, respectively (Fig. 4b)[41]. There are no obvious shift of the binding energy of the two peaks for the Fe_2O_3/MoS_2 composite, implying that the Fe_2O_3 coating has little effect on the valence states of the S species. In the Fe 2p core level spectrum for the Fe_2O_3/MoS_2 composite, the peaks at 711.3 eV, 719.2 eV and 724.8 eV represent the binding energies of Fe $2p_{3/2}$, shake-up satellite Fe $2p_{3/2}$, and Fe $2p_{1/2}$ of Fe^{3+} species, respectively (Fig. 4c)[46,47]. These values are consistent with the data of Fe_2O_3 reported by the previous literatures[48,49], confirming the existence of Fe_2O_3 in the Fe_2O_3/MoS_2 composite. Compared to the XPS spectra of Fe_2O_3 in the physical mixture $MoS_2+Fe_2O_3$, the peaks for Fe $2p_{1/2}$ and Fe $2p_{3/2}$ shift to low binding energy side, further confirming the coupling effect between Fe_2O_3 and MoS_2 in the Fe_2O_3/MoS_2 composite. The peaks 529.9 and 530.0 eV in the high-resolution XPS spectrum of O 1 s core level for the Fe_2O_3/MoS_2 composite can be assigned to oxygen in the lattice (Fe−O)[50,51] and oxygen in the lattice (Mo−O)[41], respectively (Fig. 4d). Besides, the peak at 531.5 eV is associated to the hydroxyl oxygen.
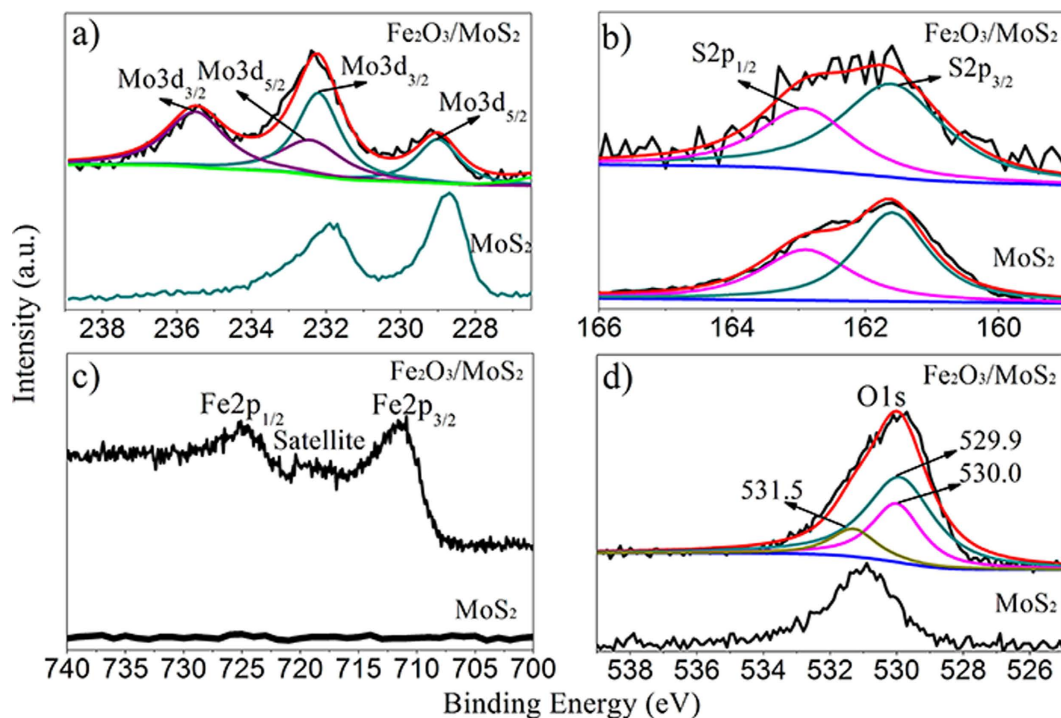
Figure 4. XPS spectra of Fe₂O₃/MoS₂ composite and MoS₂ nanosheets. (**a**) Mo 3d XPS spectrum, (**b**) S 2p XPS spectra, (**c**) Fe 2 P XPS spectrum, and (**d**) O 1 s XPS spectrum.

Cyclic voltammogram (CV) tests for coin cells of the pristine MoS_2 nanosheets were recorded at ambient temperature in the voltage range of 0.01–3 V at a scan rate of $1\,mV\,s^{-1}$ for the initial five cycles, as shown in Fig. 5a. The peak of 0.87 V in the first cathodic scanning is ascribed to the intercalation of lithium ion on different defect sites in MoS_2 to form Li_xMoS_2. In the following cathodic scanning, two new reduction peaks at approximately 1.65 V and 1.15 V are observed, which are due to the conversion of S to Li_2S and the association of Li with Mo respectively[52,53]. During the anodic scans, two peaks at 1.92 and 2.42 V are clearly observed and maintain for the subsequent sweeps, which are related to the conversion reaction of Mo and Li_2S to MoS_2 phase[54,55]. As for the pure Fe_2O_3 in Fig. 5b, the reduction peaks at 0.36 V is observed in the first cycle, and its position shifts to 0.57 V at the following scanning, which is attributed to the reduction of Fe(III) to Fe(0). In the anodic scans, the oxidation peak at 1.95 V is the oxidation of Fe to Fe_2O_3. As for the Fe_2O_3/MoS_2 composite, three reduction peaks at 0.36 V, 0.87 V and 1.20 V are observed in the first cycle (Fig. 5c). The reduction peaks locate at 0.36 V and 0.87 V during the first anodic scan can match anodic scan peaks of pure Fe_2O_3 and pure MoS_2, respectively. The peak located at 1.20 V shows a same start shoulder at ~1.05 V with pure MoS_2, which suggest the same lithiation process of MoS_2[8]. At the following scanning, however, these peaks shift to 0.65 V, 1.15 V and 1.75 V respectively. The peak at 1.15 V is related to the conversion of MoS_2 to Mo and Li_2S, while two other peaks at 1.75 and 0.65 V are attributed to the formation of $Li_xFe_2O_3$ due to the lithiation of Fe_2O_3 and the reduction of Fe(III) to Fe(0), respectively[56–60]. In the anodic scans, the oxidation peaks at 1.82 V and 2.40 V stand for oxidation of Mo to MoS_2 and Fe to Fe_2O_3, respectively. The CV results demonstrate that both Fe_2O_3 and MoS_2 in the composite contribute to the capacity of the composite. As for the physical mixture $Fe_2O_3+MoS_2$ (Fig. 5d), three reduction peaks at 0.43 V, 1.04 V and 1.30 V are found in the first cycle, and then their positions shift to 0.71 V, 1.16 V and 1.81 V after the following scanning, respectively, which are close to the positions of the corresponding peaks for Fe_2O_3/MoS_2 composite (Fig. 5c). In the anodic scans, the oxidation peaks are also in accordance with Fe_2O_3/MoS_2 composite. The observations suggest that similar electrochemical reactions occur for $Fe_2O_3+MoS_2$ and Fe_2O_3/MoS_2 composites during charging/discharging process. However, the physical mixture $Fe_2O_3+MoS_2$ has larger irreversible capacity than the Fe_2O_3/MoS_2 composite, as shown in Fig. 5c and d, suggesting advantage of coupling ultrasmall Fe_2O_3 nanoparticles with MoS_2 nanosheets. Figure 5e–h show the voltage-capacity curves of pristine MoS_2 nanosheets, pure Fe_2O_3, Fe_2O_3/MoS_2 composite and physical mixture $Fe_2O_3+MoS_2$ at a current density of $100\,mA\,g^{-1}$. The initial discharging/charging capacities of the Fe_2O_3/MoS_2 composite are $1366/1207\,mA\,h\,g^{-1}$, greatly larger than that of pure MoS_2 nanosheets ($854/754\,mAh\,g^{-1}$), pure Fe_2O_3 ($1218/879\,mAh\,g^{-1}$) and the physical mixture $Fe_2O_3+MoS_2$ ($1056/815\,mAh\,g^{-1}$). Furthermore, the Fe_2O_3/MoS_2 composite has a Coulombic efficiency of 88.4% at the first cycle, much higher than that of the physical mixture $Fe_2O_3+MoS_2$ (77.2%), consistent with the CV results. The energy efficiency (discharge energy/charge energy) of the Fe_2O_3/MoS_2 composite are 43%~58% (Figure S7). The larger specific capacity and higher Coulombic efficiency of the Fe_2O_3/MoS_2 composite indicate that coupling ultrasmall Fe_2O_3 particles with MoS_2 nanosheets is an efficient strategy to improve the electrochemical performance of the MoS_2 nanosheets.
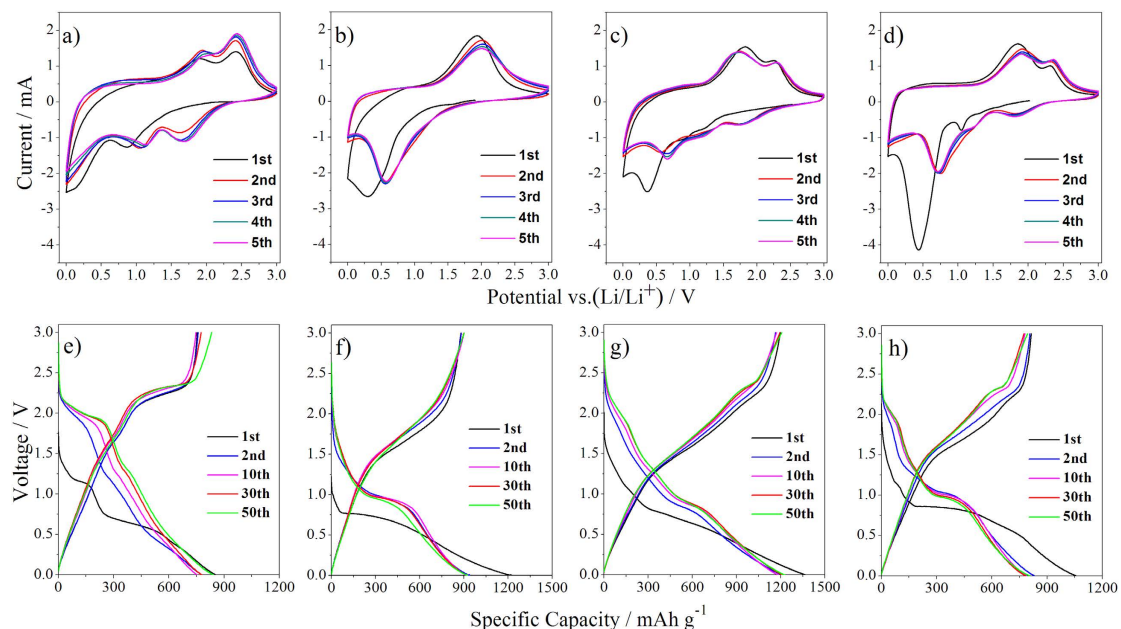
Figure 5. CV curves of (**a**) MoS_2 nanosheets, (**b**) Fe_2O_3, (**c**) Fe_2O_3/MoS_2 composite and (**d**) the physical mixture $Fe_2O_3+MoS_2$, and charging–discharging curves of (**e**) MoS_2 nanosheets, (**f**) Fe_2O_3, (**g**) Fe_2O_3/MoS_2 composite and (**h**) the physical mixture $Fe_2O_3+MoS_2$.

To confirm the superiority of the Fe_2O_3/MoS_2 composite as an anode material over the pristine MoS_2 nanosheets and the physical mixture $Fe_2O_3+MoS_2$ in the lithium storage performance, we compared their cycling behaviors at different current densities (Fig. 6). Clearly, MoS_2 nanosheets deliver an initial capacity of 854 $mAh g^{-1}$ at a current density of 100 $mA g^{-1}$ (Fig. 6a), higher than its theoretical value due to its ultra-thin nanosheets for lithium storage. However, obvious capacity decay is witnessed when cycled at a high current density (Fig. 6a). For example, the capacity decreases from 638 $mA h g^{-1}$ to 449 $mA h g^{-1}$ at 1 $A g^{-1}$ only after 40 cycles. This phenomenon is probably due to the exfoliation of the ultra-thin MoS_2 nanosheets during discharging/charging process. Similarly, the pure Fe_2O_3 delivers an initial discharge capacity of 1219 $mAh g^{-1}$ at a current densities of 100 $mA g^{-1}$, and the capacity decreases from 533 $mA h g^{-1}$ to 287 $mA h g^{-1}$ at 1 $A g^{-1}$ only after 55 cycles (Fig. 6b). As the MoS_2 nanosheets are mixed with Fe_2O_3 mechanically, slightly better cycling stability at the current densities of 100 $mA g^{-1}$ and 1 $A g^{-1}$ than the pristine MoS_2 nanosheets can be achieved, as shown in Fig. 6c. However, the physical mixture still shows poor cycling stability at a high current density. For example, the discharge capacity of the physical mixture decreases from 698 $mA h g^{-1}$ to 545 $mA h g^{-1}$ after 80 cycles at a high current density of 1 $A g^{-1}$ (Fig. 6c). In contrast, the Fe_2O_3/MoS_2 composite exhibits drastically enhanced rate capability (Fig. 6d,e and Figure S8). Furthermore, the Fe_2O_3/MoS_2 composite shows an excellent cycling durability at different current densities. For example, the Fe_2O_3/MoS_2 composite delivers an initial discharge capacity of 1366 $mAh g^{-1}$ at current densities of 100 $mA g^{-1}$. The capacity does not decay after 150 cycles, but gradually increases to 1350 $mA h g^{-1}$ with a high Coulombic efficiency of >98.7% (Fig. 6d). Surprisingly, even at high current densities of 1 and 2 $A g^{-1}$, the composite also exhibits excellent cycling stability (Fig. 6e). The capacity of the Fe_2O_3/MoS_2 composite increases from 908 $mA h g^{-1}$ to 1011 $mA h g^{-1}$ at 1 $A g^{-1}$, and from 829 $mA h g^{-1}$ to 864 $mA h g^{-1}$ at 2 $A g^{-1}$ after 140 cycles (Fig. 6e). The cycling performance is inferior to that of MoS_2/graphene composite with the capacity of 907 $mA h g^{-1}$ after 400 cycles[29], however, comparable or superior to most other Fe_2O_3 and MoS_2 or their composites, which is summarized in Table S1[8,13,21,37,61–71]. For example, the capacity of Fe_2O_3 nanoparticles was only about 300 $mAh g^{-1}$ at ca. 100 $mA g^{-1}$ after 100 cycles[37]; the capacity of CNTs–MoS_2 was 737 $mA h g^{-1}$ at 100 $mA g^{-1}$ after 30 cycles[69]. Furthermore, when the current density is increased to 5 $A g^{-1}$, the composite shows a relatively bad cycling durability, but still delivers a capacity of 481 $mA h g^{-1}$ after 140 cycles. To reveal the charge/discharge stability of anode, the SEM and elemental mapping analyses of Fe_2O_3/MoS_2 composite after 100 cycles were carried out. After the cycling, the utrasmall Fe_2O_3 nanoparticles are still resolved in the basal planes of the MoS_2 nanosheets, as shown in Figure S9. Elemental mapping images (Figure S10) reveal that Fe and Mo elements are uniformly distributed in the composite. These results above demonstrate that the Fe_2O_3/MoS_2 composite exhibit significantly enhanced capacity, rated capability and cycling stability compared to the pristine MoS_2 nanosheets, the pure Fe_2O_3 and the physical mixture $Fe_2O_3+MoS_2$. Notably, the electrochemical performance of Fe_2O_3/MoS_2 composite was measured at room temperature. It is well known that the electrochemical performance of the anode material for LIBs is suppressed significantly at the ambient temperature lower than 0 °C. However, as previously reported, the specific capacity of MoS_2/G electrode at −20 °C still remained ca. 700 $mAh g^{-1}$ at 100 $mA g^{-1}$[29]. This result indicates that MoS_2-based anode material may be used at low-temperature environment. The electrochemical performance of our Fe_2O_3/MoS_2 composite at such low-temperature environment is studied under way.
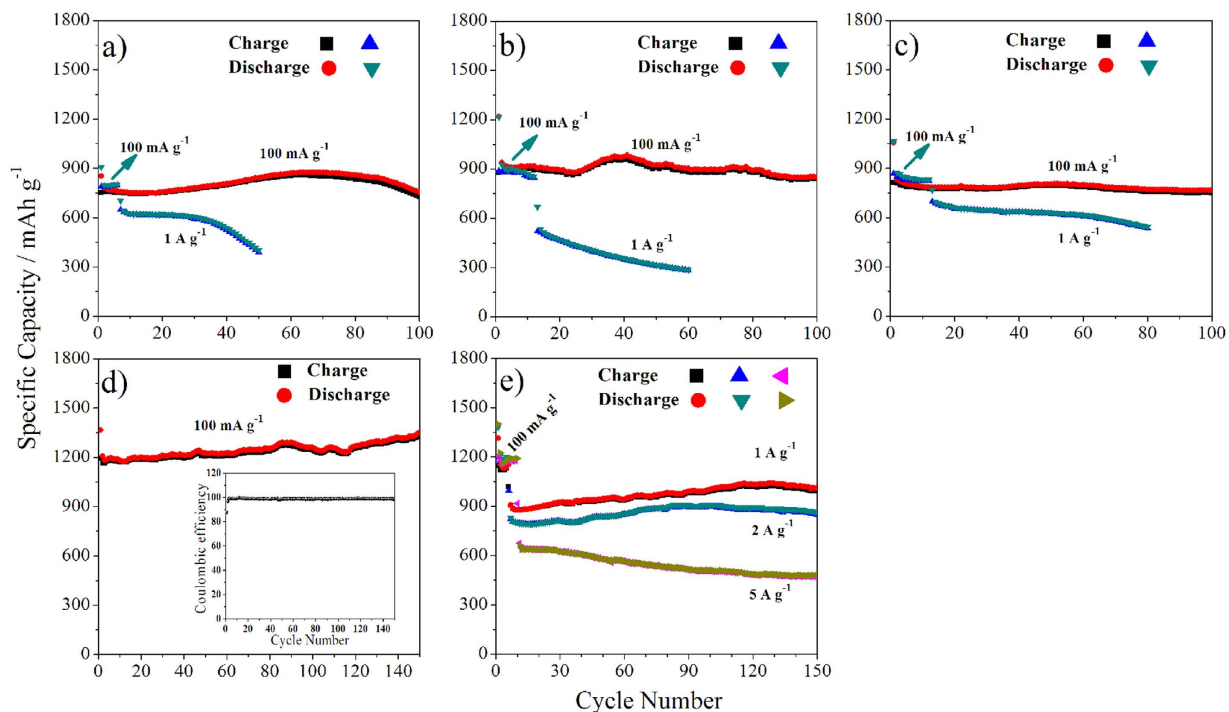
Figure 6. Cycling stability of samples at different current densities. (**a**) MoS_2 nanosheets at 100 and 1000 mA g^{-1}, (**b**) Fe_2O_3 at 100 and 1000 mA g^{-1}, (**c**) the physical mixture $Fe_2O_3+MoS_2$ at 100 and 1000 mA g^{-1}, (**d**) Fe_2O_3/MoS_2 composite at 100 mh g^{-1}, the inset showing the corresponding Coulombic efficiency and (**e**) Fe_2O_3/MoS_2 composite at 1000 mA g^{-1}, 2 000 mA g^{-1} and 5000 mA g^{-1} (initial 6 cycles at 100 mA g^{-1}).

Discussion

The excellent electrochemical properties of the Fe_2O_3/MoS_2 composite, as evidenced by a remarkably increased reversible capacity, improved rate capability, and robust long-term stability even at a high current density, indicates that the Fe_2O_3/MoS_2 composite is favorable for superior anode materials for Li-ion battery. The following factors can be attributed to the improved electrochemical properties of the Fe_2O_3/MoS_2 composite. First, unlike some designed composites[21,61,63,68,69,71], both Fe_2O_3 and MoS_2 in our composite can contribute to the total capacity of the anode, elucidated by CV measurements (Fig. 5c). The high reversible capacity of the Fe_2O_3/MoS_2 composite may also be related to its unique heteronanostructure character. As we know, during the first discharge process, Fe_2O_3 reacts with Li^+, and then Fe and Li_2O will gradually produce (Equation 1)[72]; however, only partial Li_2O can reversibly converse to Li^+ during the subsequent charging process, leading to a high irreversible capacity of Fe_2O_3-based anodes. On the other hand, during the first discharging process of MoS_2, amorphous Mo metal clusters will form (Equation 2) and disperse on the surface of MoS_2. The Mo metal clusters have highly electrochemical activity[73,74]. Considering the unique heteronanostructure of the Fe_2O_3/MoS_2 composite, the Mo metal clusters on the MoS_2 surface can efficiently contact with Li_2O and make the irreversible Li_2O converse to Li^+, as shown in Fig. 7a. As a result, the Fe_2O_3/MoS_2 composite shows a low irreversible capacity and a high Coulombic efficiency of 88.4% at the first cycle. As for the physical mixture $Fe_2O_3+MoS_2$, since the efficient contact between Mo and Li_2O is more difficultly available, the conversion of Li_2O to Li^+ will be greatly suppressed (Fig. 7b). Consequently, the physical mixture $Fe_2O_3+MoS_2$ shows a high irreversible capacity and a low Coulombic efficiency at the first cycle (Fig. 5d and h).

$$Fe_2O_3 + 6Li^+ \rightarrow Fe + Li_2O \qquad (1)$$

$$MoS_2 + 4Li^+ \rightarrow Mo + Li_2S \qquad (2)$$

Second, the average Fe_2O_3 size is approximately 4.0 nm, which can shorten the Li ion transfer length and then facilitate the improvement of the rate capability. Additionally, nitrogen adsorption–desorption isotherms show that Brunauer–Emmett–Teller (BET) surface areas and cumulative volume of pores were 12.5 m^2 g^{-1} and 0.06 cm^3 g^{-1} for the pristine nanosheets, around two times lower than those of the composite (23.1 m^2 g^{-1} and 0.12 cm^3 g^{-1}), as shown in Figure S11 and Figure S12. The bigger BET surface area and larger pore volume not only allow for fast Li-ion diffusion, but also buffer the volume changes accompanying the Li charging and discharging processes[28]. Third, the strong coupled interfaces boost a rapid interfacial charge transfer, leading to excellent rate capability of the Fe_2O_3/MoS_2 composite, as evidenced by electrochemical impedance measurements. Nyquist plots (Fig. 8) shows that the Fe_2O_3/MoS_2 composite has a charge transfer resistance (R_{ct}) of 39.9 Ω, greatly smaller than that of the physical mixture $Fe_2O_3+MoS_2$ (238.9 Ω), the pure Fe_2O_3 (136.0 Ω) and the
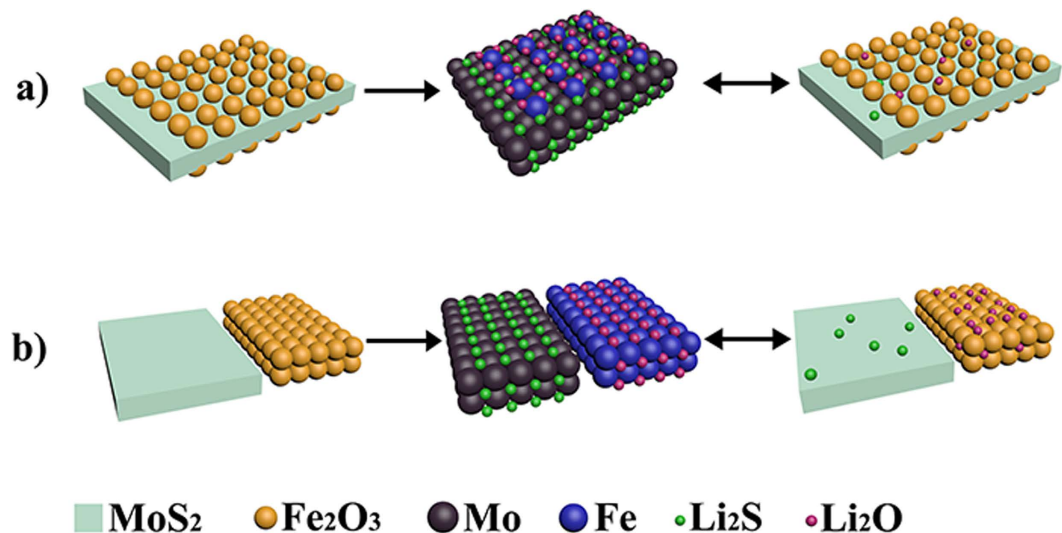
Figure 7. (**a**) Schematic illustration of the irreversible Li_2O converse to Li^+ for the Fe_2O_3/MoS_2 composite. Due to high electrochemical activity of Mo metal clusters and efficient contact between Mo metal clusters and the irreversible Li_2O, the irreversible Li_2O can converse to Li^+ after the charging process, and (**b**) Schematic illustration of the irreversible Li_2O converse to Li^+ for the physical mixture $Fe_2O_3+MoS_2$. The conversion of the irreversible Li_2O to Li^+ will be greatly suppressed because the efficient contact between Mo and Li_2O is more difficultly available.
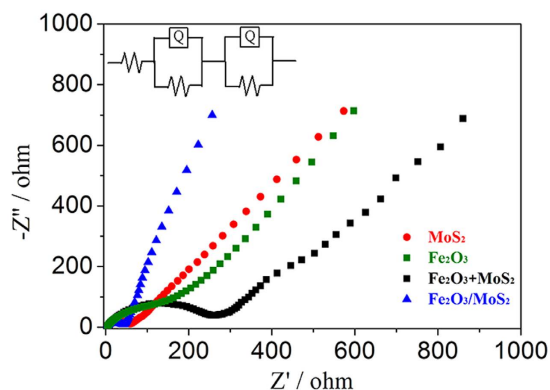

Figure 8. Nyquist plots for samples from 100 kHz to 0.01 Hz.

pristine MoS_2 nanosheets (51.3 Ω), at high frequency 100000 Hz, Low frequency 0.01 Hz and amplitude 0.005 V. The strong coupling between MoS_2 and Fe_2O_3 implies that small Fe_2O_3 nanoparticles are tightly anchored on the MoS_2 scaffolds, facilitating long-term stability of the Fe_2O_3/MoS_2 composite even at a high current density. Taken together, the synergistic effect of two excellent anode materials and the unique structural features of the composite make it an attractive candidate for anode material for Li-ion battery.

In summary, a facile and cost-effective strategy was developed to anchor ultrasmall Fe_2O_3 nanoparticles on the surface of MoS_2 nanosheets. Due to the synergistic effect of two excellent anode materials and the unique structural feature, the Fe_2O_3/MoS_2 composite exhibits excellent electrochemical properties, including a remarkably increased reversible capacity, improved rate capability, and long-term stability even at a high current density. After 140 cycles the reversible capacity of the composite does not decay, but increases from 829 mA h g^{-1} to 864 mA h g^{-1} at a high current density of 2 A g^{-1}, outperforming other MoS_2- and iron oxide-based anode materials previously reported. Thus, the facile strategy may open a way for development of cost-efficient anode material with high-performance for large-scale energy conversion and storage systems.

Methods

Synthesis of samples. MoS_2 nanosheets were first synthesized by a solution-based method[40]. Simply, $(NH_4)_6Mo_7O_{24}\cdot4H_2O$ (1 mmol) and thiourea (30 mmol) were dissolved in distilled water (35 mL) under vigorous stirring to form a homogeneous solution. After being stirred for 30 min, the solution was transferred into a 50 mL Teflon-lined stainless steel autoclave and maintained at 180 °C for 24 h. The obtained products were collected by centrifugation, washed with distilled water and ethanol, and dried at 40 °C under vacuum. The obtained MoS_2

nanosheets (30 mg) was dispersed in ethyl alcohol (75 mL) and then iron acetylacetone (0.5 mmol), distilled water (1.8 mL) and ammonia (2 mL) were added. After sonication for 15 min at room temperature the mixture was heated at 80 °C for 10 h in a water bath. The precipitates were separated by centrifugation, washed with distilled water and ethanol, and dried at 40 °C for 24 h under vacuum. The growth of ultra-small Fe_2O_3 nanoparticles on the MoS_2 nanosheets was achieved after the dried powder was thermally treated at 500 °C for 3 h under an Ar flow. For convenience, the obtained sample denoted as Fe_2O_3/MoS_2 composite. As shown in Figure S13, the Fe and Mo atom ratio was 2:1. The Fe_2O_3 was prepared by heating graphene–hollow iron oxide at 500 °C for 1.5 h under air atmosphere[72], and then was thermally treated at 350 °C for 1 h under an Ar/H_2 flow. The physical mixture Fe_2O_3 and MoS_2 (denoted as $Fe_2O_3+MoS_2$) as reference sample was prepared by grinding the MoS_2 nanosheets and commercial Fe_2O_3 powder according to Fe and Mo atomic ratio.

Structure characterizations. The morphology and size of the samples were characterized by scanning electron microscope (SEM, Hitachi SU 70) (Condition = Vacc = 15KV, Mag = x60.0k- x250k, Working Distance = 15800 um, Emission Current = 28000 nA) and a FEI Tecnai-F20 transmission electron microscope (TEM) equipped with a Gatan imaging filter (GIF), operated at an accelerating voltage of 200 kV, combined with HRTEM and EDX measurements. The crystal structure of the sample was determined by X-ray diffraction (XRD) [D/max 2550 V, Cu Kα radiation] in the 2θ range of 5–70°. (X-Ray 40 kV/100 mA, DivSlit 1 deg., RecSlit open, DivH.L.Slit 10mm, SctSlit 8.0mm, Step 0.02). X-ray photoelectron spectra (XPS) were carried out by using a spectrometer with Mg Kα radiation (PHI 5700 ESCA System). The binding energy was calibrated with the C 1 s position of contaminant carbon in the vacuum chamber of the XPS instrument (284.6 eV). The pore diameter distribution and surface area were tested by nitrogen adsorption/desorption analysis (TRISTAR II3020).

Electrochemical measurements. The electrochemical tests were performed at ambient temperature using two-electrode coin cells (CR 2016) with lithium foils serving as the counter electrode. The active material was mixed with a conductive acetylene black, and a commercial polymer binder (LA133) at a weight ratio of 70:15:15. The mixture was painted onto a Cu foil and dried in air, then cut into 14 mm diameters of round piece. Finally the electrode pieces were dried in vacuum at 60 °C for 12 h to adequately evaporate the residual moisture. The average thickness and mass loading of the electrode were ~3.5 μm (Figure S14) and 1.5 ± 0.2 mg, respectively. The electrolyte was made of $LiPF_6$ (1 M) in a mixture of ethylene carbonate (EC) and dimethyl carbonate (DMC) with the volume ratio 1:1. The 2016 coin-type cells were assembled in an Ar filled glove box, and pure Li foils were used as the counter electrodes. The charge–discharge cycles were carried out on a battery measurement system (LAND-BT2013A) at various current densities of 100–5000 mA g^{-1} in the cutoff voltage range of 3 to 0 V versus Li/Li$^+$ at room temperature (~20 °C). Cyclic voltammetry measurements were carried out on a CHI660D electrochemical workstation over the potential range of 3.0 to 0.01 V at a scan rate of 1 mV s^{-1}.

References

1. Armand, M. & Tarascon, J. M. Building better batteries. *Nature* **451,** 652–657 (2008).
2. Tarascon, J. M. & Armand, M. Issues and challenges facing rechargeable lithium batteries. *Nature* **414,** 359–367 (2001).
3. Wang, L. F., Xu, Z., Wang, W. L. & Bai, X. D. Atomic mechanism of dynamic electrochemical lithiation processes of MoS_2 nanosheets. *J. Am. Chem. Soc.* **136,** 6693–6697 (2014).
4. Wang, Q. & Li, J. H. Facilitated lithium atorage in MoS_2 overlayers supported on coaxial carbon nanotubes. *J Phys. Chem. C* **111,** 1675–1682 (2007).
5. Yu, X. Y., Yu, L. & Lou, X. W. Metal sulfide hollow nanostructures for electrochemical energy storage. *Adv. Energy Mater.* **6,** 1501333 (2016).
6. Liu, H. *et al.* Highly ordered mesoporous MoS_2 with expanded spacing of the (002) crystal plane for ultrafast lithium ion storage. *Adv. Energy Mater.* **2,** 970–975 (2012).
7. Sen, U. K. & Mitra, S. High-rate and high-energy-density lithium-ion battery anode containing 2D MoS_2 nanowall and cellulose binder. *ACS Appl. Mater. Interfaces* **5,** 1240–1247 (2013).
8. Sun, P. L. *et al.* Synthesis of hierarchical MoS_2 and its electrochemical performance as an anode material for lithium-ion batteries. *J. Mater. Chem. A* **2,** 3498–3504 (2014).
9. Stephenson, T., Li, Z., Olsen, B. & Mitlin, D. Lithium ion battery applications of molybdenum disulfide (MoS_2) nanocomposites. *Energy Environ. Sci.* **7,** 209–231 (2014).
10. Xiao, J. *et al.* Exfoliated MoS_2 nanocomposite as an anode material for lithium ion batteries. *Chem. Mater.* **22,** 4522–4524 (2010).
11. Wang, P. P., Sun, H. Y., Ji, Y. J., Li, W. H. & Wang, X. Three-dimensional assembly of single-layered MoS_2. *Adv. Mater.* **26,** 964–969 (2014).
12. Li, G. D. *et al.* Facile synthesis of hierarchical hollow MoS_2 nanotubes as anode materials for high-performance lithium-ion batteries. *CrystEngComm* **16,** 10754–10759 (2014).
13. Zhang, L., Wu, H. B., Yan, Y., Wang, X. & Lou, X. W. Hierarchical MoS_2 microboxes constructed by nanosheets with enhanced electrochemical properties for lithium storage and water splitting. *Energy Environ. Sci.* **7,** 3302–3306 (2014).
14. Yu, X. Y., Hu, H., Wang, Y. W., Chen, H. Y. & Lou, X. W. Ultrathin MoS_2 nanosheets supported on N-doped carbon nanoboxes with enhanced lithium storage and electrocatalytic properties. *Angew. Chem. Int. Ed.* **54,** 7395–7398 (2015).
15. Ko, Y. N., Kang, Y. C. & Park, S. B. Superior Electrochemical properties of MoS_2 powders with a MoS_2@void@ MoS_2 configuration. *Nanoscale* **6,** 4508–4512 (2014).
16. Ding, S., Zhang, D., Chen, J. S. & Lou, X. W. Facile synthesis of hierarchical MoS_2 microspheres composed of few-layered nanosheets and their lithium storage properties. *Nanoscale* **4,** 95–98 (2012).
17. Wang, M., Li, G., Xu, H. Y. & Qian, Y. T., Yang, J. Enhanced lithium storage performances of hierarchical hollow MoS_2 nanoparticles assembled from nanosheets. *ACS Appl. Mater. Interfaces* **5,** 1003–1008 (2013).
18. Wang, Z. *et al.* CTAB-assisted synthesis of single-layer MoS_2–graphene composites as anode materials of li-ion batteries. *J. Mater. Chem. A* **1,** 2202–2210 (2013).
19. Pham, V. H. *et al.* Liquid phase Co-exfoliated MoS_2 egraphene composites as anode materials for lithium ion batteries. *J. Power Sources* **244,** 280–286 (2013).
20. Hou, Y. *et al.* N-doped graphene/porous g-C_3N_4 nanosheets supported layered- MoS_2 hybrid as robust anode materials for lithium-ion batteries. *Nano Energy* **8,** 157–164 (2014).

21. Huang, G. C. *et al.* Graphene-like MoS₂/graphene composites: cationic surfactant-assisted hydrothermal synthesis and electrochemical reversible storage of lithium. *Small* **9,** 3693–3703 (2013).
22. Cao, X. H. *et al.* Preparation of MoS₂-coated three-dimensional graphene networks for high-performance anode material in lithium-ion batteries. *Small* **9,** 3433–3438 (2013).
23. Zhou, X. S., Wan, L. J. & Guo, Y. G. Synthesis of MoS₂ nanosheet–graphene nanosheet hybrid materials for stable lithium storage. *Chem. Commun.* **49,** 1838–1840 (2013).
24. Xiao, J. *et al.* Electrochemically induced high capacity displacement reaction of PEO/MoS₂/graphene nanocomposites with lithium. *Adv. Funct. Mater.* **21,** 2840–2846 (2011).
25. Li, H. L. *et al.* MoS₂/graphene hybrid nanoflowers with enhanced electrochemical performances as anode for lithium-ion batteries. *J. Phys. Chem. C* **119,** 7959–7968 (2015).
26. Wang, R. H. *et al.* Heat-induced formation of porous and free-standing MoS₂/GS hybrid electrodes for binder-free and ultralong-life lithium ion batteries. *Nano Energy* **8,** 183–195 (2014).
27. Ma, L., Ye, J. B., Chen, W. X., Chen, D. Y. & Lee, J. Y. Gemini surfactant assisted hydrothermal synthesis of nanotile-like MoS₂/graphene hybrid with enhanced lithium storage performance. *Nano Energy* **10,** 144–152 (2014).
28. Yu, H. L. *et al.* Three-dimensional hierarchical architectures constructed by graphene/MoS₂ nanoflake arrays and their rapid charging/discharging properties as lithium-ion battery anodes. *Chem. –Eur. J.* **19,** 5818–5823 (2013).
29. Teng, Y. Q. *et al.* MoS₂ Nanosheets vertically grown on graphene sheets for lithium-ion battery anodes. *ACS Nano* **10,** 8526–8535 (2016).
30. Zhu, C. B., Mu, X. K., Aken, P. A., Maier, J. & Yu, Y. Fast Li storage in MoS₂-graphene-carbon nanotube nanocomposites: advantageous functional integration of 0D, 1D, and 2D nanostructures. *Adv. Energy Mater.* **5,** 1401170 (2015).
31. Wang, J. Z. *et al.* Development of MoS₂–CNT composite thin film from layered MoS₂ for lithium batteries. *Adv. Energy Mater.* **3,** 798–805 (2013).
32. Kartick, B., Suneel Kumar, S. & Sourindra, M. MoS₂–MWCNT hybrids as a superior anode in lithium-ion batteries. *Chem. Commun.* **49,** 1823–1825 (2013).
33. Zhang, L. & Lou, X. W. Hierarchical MoS₂ shells supported on carbon spheres for highly reversible lithium storage. *Chem.–Eur. J.* **20,** 5219–5223 (2014).
34. Yu, H. L. *et al.* Three-dimensional hierarchical MoS₂ nanoflake array/carbon cloth as high-performance flexible lithium-ion battery anodes. *J. Mater. Chem. A* **2,** 4551–4557 (2014).
35. Zhao, C. Y. *et al.* Thin MoS₂ nanoflakes encapsulated in carbon nanofibers as highperformance anodes for lithium-ion batteries. *ACS Appl. Mater. Interfaces* **6,** 6392–6398 (2014).
36. Xu, X. *et al.* A nanosheets-on-channel architecture constructed from MoS₂ and CMK-3 for high-capacity and long-cycle-life lithium storage. *Adv. Energy Mater.* **4,** 1400902 (2014).
37. Lupo, F. D. *et al.* α- Fe₂O₃ lithium battery anodes by nanocasting strategy from ordered 2D and 3D templates. *J. Alloys Compd.* **615,** S482–S486 (2014).
38. Cao, Z. Y. & Wei, B. Q. α- Fe₂O₃/single-walled carbon nanotube hybridfilms as highperformance anodes for rechargeable lithium-ion batteries. *J. Power Sources* **241,** 330–340 (2013).
39. Wang, Y. G., Li, H. Q., He, P., Hosono, E. & Zhou, H. S. Nano active materials for lithium-ion batteries. *Nanoscale* **2,** 1294–1305 (2010).
40. Bruce, P. G., Scrosati, B. & Tarascon, J.-M. Nanomaterials for rechargeable lithium batteries. *Angew. Chem. Int. Ed.* **47,** 2930–2946 (2008).
41. Xie, J. F. *et al.* Controllable disorder engineering in oxygen-incorporated MoS₂ ultrathin nanosheets for efficient hydrogen evolution. *J. Am. Chem. Soc.* **135,** 17881–17888 (2013).
42. Yu, H. L. *et al.* A strategy to synergistically increase the number of active edge sites and the conductivity of MoS₂ nanosheets for hydrogen evolution. *Nanoscale* **7,** 8731–8738 (2015).
43. Baker, M. A., Gilmore, R., Lenardi, C. & Gissler, W. XPS Investigation of preferential sputtering of S from MoS and 2 determination of MoS stoichiometry from Mo and S peak x positions. *Appl. Surf. Sci.* **150,** 255–262 (1999).
44. Wang, H. W., Skeldon, P. & Thompson, G. E. XPS studies of MoS₂ formation from ammonium tetrathiomolybdate solutions. *Surf. Coat. Technol.* **91,** 200–207 (1997).
45. Lin, T. R., Wang, J., Guo, L. Q. & Fu, F. F. Fe₃O₄@ MoS₂ core–shell composites: preparation, characterization, and catalytic application. *J. Phys. Chem. C* **119,** 13658–13664 (2015).
46. Jiang, Y. Z. *et al.* Amorphous Fe₂O₃ as a high-capacity, high-rate and long-life anode material for lithium ion batteries. *Nano Energy* **4,** 23–30 (2014).
47. Biesinger, M. C. *et al.* Resolving surface chemical states in XPS analysis of first row transition metals, oxides and hydroxides: Cr, Mn, Fe, Co and Ni. *Appl. Surf. Sci.* **257,** 2717–2730 (2011).
48. Xiong, Y. H. *et al.* Synthesis of magnetic porous g-Fe₂O₃/C@HKUST-1 composites for efficient removal of dyes and heavy metal ions from aqueous solution. *RSC Adv.* **5,** 5164–5172 (2015).
49. Fujii, T., De Groot, F. M. F. & Sawatzky, G. A. *In situ* XPS analysis of various iron oxide films grown by NO₂-assisted molecular-beam epitaxy. *Phys. Rev. B* **59,** 3195–3202 (1999).
50. Sun, M., Dong, Y. Z., Zhang, G., Qu, J. H. & Li, J. H. α- Fe₂O₃ spherical nanocrystals supported on CNTs as efficient non-noble electrocatalyst for oxygen reduction reaction. *J. Mater.Chem. A* **2,** 13635–13640 (2014).
51. Pradhan, G. K., Padhi, D. K. & Parida, K. M. Fabrication of α- Fe₂O₃ nanorod/rgo composite: a novel hybrid photocatalyst for phenol degradation. *ACS Appl. Mater. Interfaces* **5,** 9101–9110 (2013).
52. Lu, Y. T. *et al.* MoS₂ nanoflowers consisting of nanosheets with a controllable interlayer distance as highperformance lithium ion battery anodes. *RSC Adv.* **5,** 7938–7943 (2015).
53. Fang, X. P. *et al.* Lithium storage in commercial MoS₂ in different potential ranges. *Electrochim. Acta* **81,** 155–160 (2012).
54. Hwang, H., Kim, H. & Cho, J. MoS₂ nanoplates consisting of disordered graphene-like layers for high rate lithium battery anode materials. *Nano Lett.* **11,** 4826–4830 (2011).
55. Chang, K. & Chen, W. X. L-cysteine-assisted synthesis of layered MoS₂/graphene composites with excellent electrochemical performances for lithium ion batteries. *ACS Nano* **5,** 4720–4728 (2011).
56. Ye, J., Zhang, J., Wang, F. X., Su, Q. M. & Du, G. H. One-potsynthesis of Fe₂O₃/graphene and its lithium-storage performance. *Electrochim. Acta* **113,** 212–217 (2013).
57. Liu, J. L. *et al.* Three dimensionals α- Fe₂O₃/polypyrrole (ppy) nanoarray as anode for micro lithium ion batteries. *Nano Energy* **2,** 726–732 (2013).
58. Zhou, G. W. *et al.* Facile spray drying route for the three-dimensional graphene encapsulated Fe₂O₃ nanoparticles for lithium ion battery anodes. *Ind. Eng. Chem. Res.* **52,** 1197–1204 (2013).
59. Xu, S. M. *et al.* α-Fe₂O₃ multi-shelled hollow microspheres for lithium ion battery anodes with superior capacity and charge retention. *Energy Environ. Sci.* **7,** 632–637 (2014).
60. Gao, G. X., Yu, L., Wu, H. B. & Lou, X. W. Hierarchical tubular structures constructed by carboncoated α-Fe₂O₃ nanorods for highly reversible lithium storage. *Small* **9,** 1741–1745 (2013).
61. Zhu, X. D. *et al.* Creating a synergistic interplay between tubular MoS₂ and particulate Fe₃O₄ for improved lithium storage. *Chem. Commun.* **51,** 11888–11891 (2015).

62. Chen, Y., Song, B. H., Tang, X. H., Lu, L. & Xue, J. M. Ultrasmall Fe$_3$O$_4$ nanoparticle/MoS$_2$ nanosheet composites with superior performances for lithium ion batteries. *Small* **10,** 1536–1543 (2014).
63. Pan, L., Zhu, X. D., Xie, X. M. & Liu, Y. T. Delicate ternary heterostructures achieved by hierarchical Co-assembly of Ag and Fe$_3$O$_4$ nanoparticles on MoS$_2$ nanosheets: morphological and compositional synergy in reversible lithium storage. *J. Mater. Chem. A* **3,** 2726–2733 (2015).
64. Wan, Z. M. *et al.* Core–shell structure of hierarchical quasi-hollow MoS$_2$ microspheres encapsulated porous carbon as stable anode for li-ion batteries. *Small* **10,** 4975–4981 (2014).
65. Lu, L. *et al.* Monolithic Fe$_2$O$_3$/graphene hybrid for highly efficient lithium storage and arsenic removal. *Carbon* **67,** 500–507 (2014).
66. Zhang, L., Wu, H. B., Madhavi, S., Hng. H. H. & Lou, X. W. Formation of Fe$_2$O$_3$ microboxes with hierarchical shell structures from metal–organic frameworks and their lithium storage properties. *J. Am. Chem. Soc.* **134,** 17388–17391 (2012).
67. Pan, L., Liu, Y. T., Xie, X. M. & Zhu, X. D. Coordination-driven hierarchical assembly of silver nanoparticles on MoS$_2$ nanosheets for improved lithium storage. *Chem. Asian J.* **9,** 1519–1524 (2014).
68. Xu, X., Fan, Z. Y., Ding, S. J., Yu, D. M. & Du, Y. P. Fabrication of MoS$_2$ nanosheet@TiO$_2$ nanotube hybrid nanostructures for lithium storage. *Nanoscale* **6,** 5245–5250 (2014).
69. Park, S. K. *et al.* A simple l-cysteine-assisted method for the growth of MoS$_2$ nanosheets on carbon nanotubes for high-performance lithium ion batteries. *Dalton Trans.* **42,** 2399–2405 (2013).
70. Han, S. *et al.* Ternary MoS$_2$/SiO$_2$/graphene hybrids for high-performance lithium storage. *Carbon* **81,** 203–209 (2015).
71. Liu, H. *et al.* Porous tremella-like MoS$_2$/polyaniline hybrid composite with enhanced performance for lithium-ion battery anodes. *Electrochim. Acta* **167,** 132–138 (2015).
72. Yu, X. B. *et al.* Growth of hollow transition metal (Fe, Co, Ni) oxide nanoparticles on graphene sheets through kirkendall effect as anodes for high-performance lithium-ion batteries. *Chem. –Eur. J.* **22,** 1638–1645 (2016).
73. Poizot, P., Laruelle, S., Grugeon, S., Dupont, L. & Tarascon, J.-M. ChemInform abstract: nano-sized transition-metal oxides as negative-electrode materials for lithium-ion batteries. *Nature* **407,** 496–499 (2000).
74. Hassan, M. F., Guo, Z. P., Chen, Z. & Liu, H. K. Carbon-coated MoO$_3$ nnanobelts as anode materials for lithium-ion batteries. *J. Power Sources* **195,** 2372–2376 (2010).

Acknowledgements

Author Contributions

Y.C. and C.L. proposed the research direction and guided the project. B.Q. designed and performed the experiments. Y.C., B.Q. and C.L. analysed and discussed the experimental results and drafted the manuscript. X.Z. carried out TEM measurements. L.L., Y.S. and C.Y. carried out some supporting experiments. All authors have read and approved the final manuscript.

Additional Information

Supplementary information accompanies this paper at http://www.nature.com/srep

Competing financial interests: The authors declare no competing financial interests.

How to cite this article: Qu, B. *et al.* Ultrasmall Fe$_2$O$_3$ nanoparticles/MoS$_2$ nanosheets composite as high-performance anode material for lithium ion batteries. *Sci. Rep.* **7,** 42772; doi: 10.1038/srep42772 (2017).

Publisher's note: Springer Nature remains neutral with regard to jurisdictional claims in published maps and institutional affiliations.